

Siamese Neural Network for Label-Efficient Critical Phenomena Prediction in 3D Percolation Models

Shanshan Wang¹, Dian Xu¹, Jianmin Shen^{1,2}, Feng Gao¹, Wei Li^{1,3}, and Weibing Deng^{1,*}

¹Key Laboratory of Quark and Lepton Physics (MOE) and Institute of Particle Physics, Central China Normal University, Wuhan 430079, China

²School of engineering and technology, Baoshan University, Baoshan 678000, China

³Ecole Supérieure d'Informatique Electronique Automatique, Ivry-sur-Seine 94200, France

*wdeng@mail.ccnu.edu.cn

ABSTRACT

Percolation theory serves as a cornerstone for investigating phase transitions and critical phenomena, with profound implications across statistical physics, materials engineering, and complex networks. However, existing machine learning frameworks for percolation analysis predominantly focus on two-dimensional systems, which inherently oversimplify the intricate spatial correlations and cluster formation and morphological evolution characteristic of realistic three-dimensional materials. To bridge this methodological gap while addressing the computational scalability and annotation efficiency challenges in 3D systems, we employ a Siamese Neural Network (SNN) architecture that explicitly leverages features of the largest cluster as discriminative input. Our approach demonstrates remarkable predictive accuracy for both site and bond percolation thresholds and critical exponents in three dimensions, achieving sub-1% error margins while requiring significantly fewer labeled training samples compared to conventional methods. This paradigm shift not only establishes a robust framework for high-dimensional critical phenomenon modeling but also unlocks transformative potential in precision materials discovery and topological network characterization. The methodology's dual advantages in computational efficiency and data economy promise significant cross-disciplinary impacts, particularly in the computational design of functional materials and the analysis of emergent behaviors in complex networks.

1. Introduction

The advent of machine learning (ML) has revolutionized scientific inquiry by enabling unprecedented modeling of complex systems across scales, from quantum materials to astrophysical networks^{1,2}. Beyond its transformative impact on industrial paradigms—evident in autonomous systems³, personalized medicine⁴, and algorithmic finance⁵—ML is reshaping fundamental physics research by addressing long-standing challenges in statistical mechanics and phase transition theory^{6,7}. Specifically, ML methodologies offer a paradigm shift by transcending the limitations of traditional analytical frameworks, enabling novel insights into emergent phenomena, and simultaneously complementing conventional computational and experimental methods^{8,9}. This synergy between data-centric algorithms and physical principles not only enhances predictive accuracy but also unveils hidden patterns in complex systems, establishing ML as an indispensable tool for modern theoretical physics.

Phase transitions, as cornerstones of statistical and condensed matter physics, have traditionally been analyzed through theoretical frameworks and numerical simulations^{10,11}. While Monte Carlo (MC) methods have yielded critical insights into low-dimensional systems, their computational demands and scaling limitations become prohibitive in high dimensions ($d > 2$), where critical fluctuations span non-trivial length scales^{12,13}. This challenge has catalyzed the integration of ML, particularly deep learning architectures, into phase transition studies. Contemporary research demonstrates ML's transformative potential in predicting critical phenomena and elucidating non-equilibrium dynamics, surpassing conventional methods in efficiency and accuracy^{14,15}. Notable examples include supervised neural network classifications of phases in the 2D Ising model¹⁶, demonstrating that ML models can learn physically meaningful features directly from raw spin configurations, even without prior specification of traditional order parameters.

Percolation theory, a canonical model for disordered systems, finds broad applications in critical phenomena and material science^{17,18}. Historically, critical exponent estimation relied on MC sampling and renormalization group (RG) techniques¹⁹. However, the advent of ML has introduced paradigm-shifting capabilities: deep learning frameworks now enable high-throughput analysis of percolation configurations, achieving unprecedented precision in critical point localization while reducing computational overhead²⁰. These advancements are particularly significant for three-dimensional (3D) models, where traditional methods face severe scalability constraints, as finite-size effects and sampling inefficiencies limit their resolution and precision in critical behavior estimation. By encoding physical symmetries into latent spaces, ML circumvents the curse of

dimensionality, offering a scalable solution to the long-standing problem of high-dimensional criticality prediction.

Recent advancements in ML have catalyzed a paradigm shift in statistical physics research, particularly in the analysis of phase transitions across supervised, unsupervised, and semi-supervised learning frameworks:

1) Supervised learning for phase discrimination. The synergy between deep learning and RG theory has enabled breakthroughs in identifying topological phase transitions. CNNs have been deployed to resolve nuanced phase boundaries in the 2D Ising model through RG-inspired architectures²¹. This approach was extended to the XY model, where supervised classification successfully captured both the Berezinskii-Kosterlitz-Thouless (BKT) transition and percolation threshold behaviors by encoding spin configurations as input features²². The methodology further scaled to 3D Ising systems, demonstrating CNNs' capacity to generalize across dimensionalities while maintaining thermodynamic consistency²³.

2) Unsupervised learning for label-free phase detection. To circumvent the reliance on labeled data—a significant bottleneck in condensed matter simulations—researchers have turned to unsupervised techniques. Siamese neural Networks (SNNs) have enabled unsupervised identification of phase boundaries in both Monte Carlo simulations and Rydberg atom arrays, revealing multiple phases without prior labeling or knowledge of their existence²⁴. Principal component analysis (PCA) has enabled dimensionality reduction for Ising model phase classification, revealing hidden structures in magnetization landscapes²⁵. A notable advancement is the use of unsupervised learning methods—such as principal component analysis and variational autoencoders—for identifying phase transitions in Ising and XY models without prior knowledge of the Hamiltonian or order parameter. These approaches reveal clustered latent representations that correspond to distinct phases, enabling label-free detection of critical behavior²⁶.

3) Semi-Supervised Learning for Transferable Criticality. Semi-supervised approaches, particularly domain adversarial neural Networks (DANNs), have emerged as pivotal tools for transfer learning in phase transition studies. Notably, DANNs have been successfully applied to both equilibrium and nonequilibrium models—specifically, 2D percolation and directed percolation—demonstrating that reliable critical point prediction can be achieved with only a small, automatically selected set of labeled configurations²⁷. This framework's robustness was validated in 3D Potts models with varying q -state symmetries, where data collapse techniques confirmed that DANN accurately captured critical behavior and generalized across universality classes^{28,29}.

Despite these advancements, traditional supervised classifiers often require manually engineered order parameters and large labeled datasets, limiting their applicability in high-dimensional systems. To address these limitations, we introduce a SNN-based approach for phase transition prediction in 3D percolation models. Unlike CNNs, which rely on extensive training sets, SNNs leverage metric learning to embed percolation configurations into a latent space, where geometrical similarity between embeddings reflects proximity in phase space (e.g., closeness to the critical point).

The key contributions of this work are: (1) Few-Shot Learning Efficiency. By training on small labeled subsets sampled from non-critical regions (e.g., 100 configurations at $p \in [0, 0.1] \cup [0.9, 1]$) across multiple system sizes, SNNs accurately infer critical behavior near the transition point, significantly reducing labeling requirements compared to traditional supervised models. (2) High-Dimensional Scalability. The architecture explicitly models spatial correlations via depth-first search (DFS)-extracted largest cluster features, enabling accurate prediction of both critical thresholds and critical exponents, in agreement with established literature³⁰. (3) Impact of Labeling Interval Extension. Further experiments show that expanding the labeling interval does not significantly improve prediction accuracy, reinforcing the efficiency of SNN in handling models with limited labeled data. This finding underscores the potential of SNN for performing criticality prediction with minimal computational overhead and labeling cost.

The remainder of this paper is organized as follows: Section 2 formalizes the 3D percolation model and finite-size scaling (FSS) relations. Section 3 details the SNN architecture, contrastive learning formulation, and DFS-based feature extraction. Section 4 presents experimental results, including ablation studies on labeled data size, labeling interval extensions, and evaluation across site and bond percolation models. Section 5 concludes with implications for high-throughput materials discovery and open challenges in few-shot phase transition learning.

2. Percolation Models

The percolation model, originally developed to investigate fluid flow through porous media such as coal seams, has since become a foundational framework in modern network theory, particularly in the study of resilience, epidemic spreading, and connectivity in complex networks^{31,32}. In this context, it describes the stochastic addition or removal of nodes and edges, thereby capturing topological transitions in complex systems³³. Within statistical physics, percolation serves as a paradigmatic model for analyzing phase transitions and critical phenomena, with applications spanning condensed matter physics, materials science, and the dynamics of complex networks^{34,35}.

In a lattice system, each site (or bond) exists in one of two states: occupied or vacant. Such configurations constitute random disordered systems. When adjacent occupied sites form a connected component via nearest-neighbor adjacency, they constitute a cluster. As the occupation probability p increases, the system transitions from a fragmented state of isolated clusters to a

connected state where at least one macroscopic cluster spans the entire lattice. This transition occurs at the critical occupation probability p_c , known as the percolation threshold.

The critical behavior of the system is characterized by the order parameter $P_\infty(p)$, defined as the probability that a randomly selected site (or bond) belongs to the infinite percolation cluster at occupation probability p . Near p_c , $P_\infty(p)$ exhibits a power-law singularity:

$$P_\infty(p) \propto (p - p_c)^\beta, \quad \text{for } p \rightarrow p_c^+, \quad (1)$$

where β is the critical exponent that governs the scaling behavior of the order parameter near the percolation threshold.

In finite-size systems, the size of the largest cluster, S_{\max} , is a key observable for understanding critical behavior³⁶. As the occupation probability p approaches the critical threshold p_c , the size of the largest cluster S_{\max} increases sharply due to the emergence of long-range correlations, but remains finite owing to the system's limited size. For $p > p_c$, the largest cluster approximates the infinite percolation cluster in the thermodynamic limit. Its size in finite systems follows a FSS relation governed by the critical exponents β and ν :

$$S_{\max} \sim L^{d-\frac{\beta}{\nu}} \cdot f\left((p - p_c)L^{1/\nu}\right), \quad (2)$$

where L is the system size, L^d is the spatial dimension, and $f(x)$ is a universal scaling function. Here, ν characterizes the divergence of the correlation length near p_c , while β governs the scaling of the order parameter $P_\infty(p)$.

The site and bond percolation models studied in this work are defined on a regular three-dimensional cubic lattice^{36,37}. Figures 1 and 2 illustrate typical configurations of the site and bond percolation models on a three-dimensional cubic lattice at various occupation probabilities p . These figures demonstrate that as p increases, the largest cluster grows rapidly and eventually spans the entire lattice when $p > p_c$, signaling the emergence of a spanning cluster.

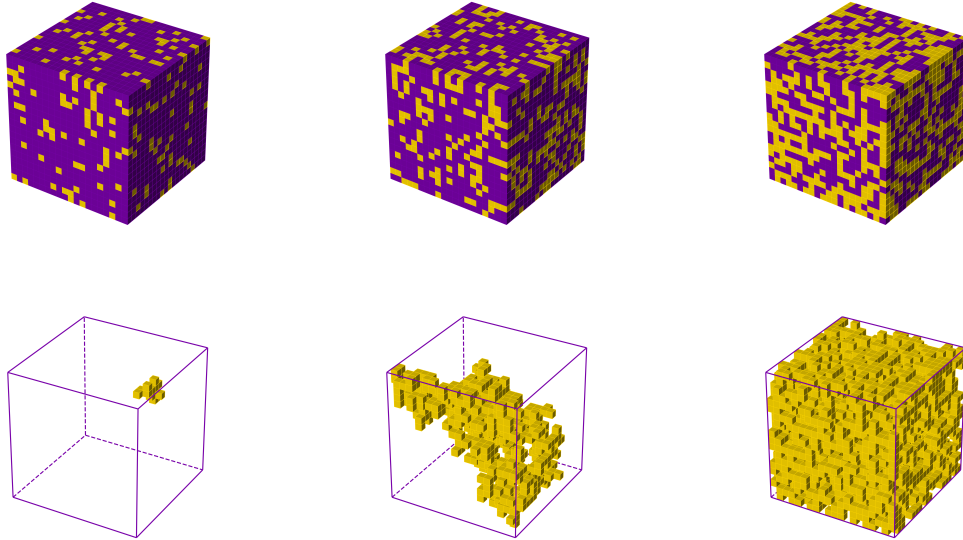


Figure 1. Site percolation on a three-dimensional cubic lattice. Top: Raw configurations at occupation probabilities $p = 0.15$, $p = 0.312$ (near the critical threshold $p_c \approx 0.3116$ for this system size), and $p = 0.47$. Bottom: Corresponding largest connected clusters, illustrating the transition from isolated clusters to a macroscopic spanning structure as p increases. The system size is $L = 20$. Occupied sites are shown; vacant sites are omitted for visual clarity.

3. Siamese Neural Network

SNNs^{38–40} were originally introduced by Bromley in 1993 for signature verification tasks, with the primary goal of learning a similarity metric between input pairs. An SNN typically consists of two identical feedforward networks that share weights and

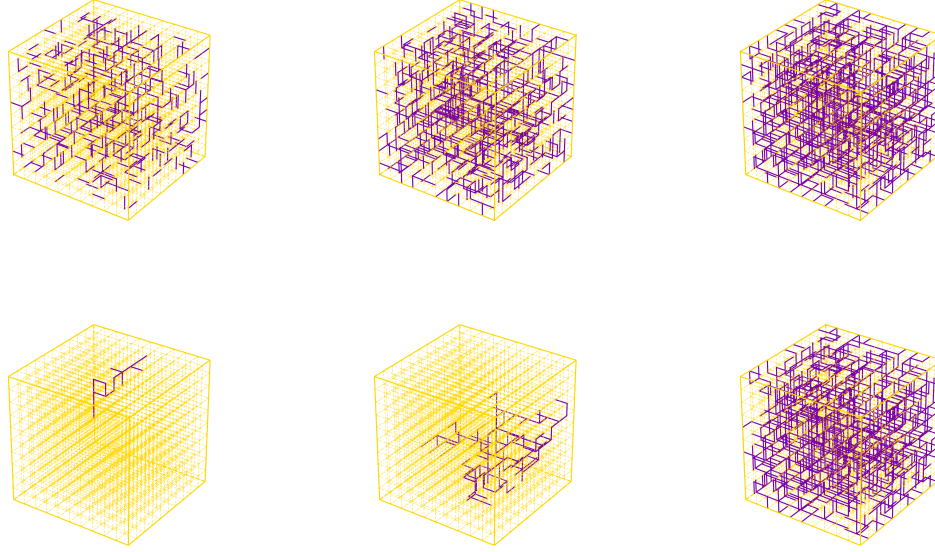


Figure 2. Bond percolation on a three-dimensional cubic lattice. Top: Raw configurations at occupation probabilities $p = 0.12$, $p = 0.249$ (near the critical threshold $p_c \approx 0.2488$ for this system size), and $p = 0.38$. Bottom: Corresponding largest connected clusters, illustrating the emergence of a macroscopic spanning structure as p increases. The system size is $L = 10$. Occupied (“open”) bonds are shown in red; vacant (“closed”) bonds are omitted for visual clarity.

process paired inputs in parallel. The similarity between inputs is evaluated by computing the distance between their output embeddings, using metrics such as Euclidean or cosine distance. During training, the network is optimized using a contrastive or triplet loss, which encourages similar pairs to produce nearby embeddings and dissimilar pairs to remain distant. SNNs have been widely applied in face recognition⁴¹, image retrieval³⁰, and audio representation⁴², particularly in scenarios involving limited labeled data or large category spaces. In this work, we employ a dual-input SNN to measure the similarity between configuration pairs in three-dimensional percolation models.

SNN Architecture for Percolation Model Analysis

As illustrated in Figure 3, the SNN architecture designed for identifying critical points in percolation models comprises two parallel fully connected neural networks (FCNNs) as feature extractors, followed by a similarity evaluator. Each FCNN branch consists of two fully connected layers, each followed by batch normalization (BatchNorm) and an activation function. The architecture of each branch is formalized as:

$$\{\text{Fl} - \text{FC}(128) - \text{B} - \text{Ac}(\text{Swish}) - \text{FC}(32) - \text{B} - \text{Ac}(\text{Sigmoid})\}, \quad (3)$$

Here, Fl represents the Flatten layer, which reshapes the input data into a one-dimensional vector for downstream processing. FC(n) refers to a fully connected layer containing n neurons, B stands for the BatchNormalization layer, which stabilizes training by normalizing intermediate activations, Ac(name) indicates the activation function applied, such as Swish or Sigmoid.

The similarity evaluator takes the concatenated embeddings from the two FCNN branches and maps them through:

$$\{\text{FC}(32) - \text{B} - \text{Ac}(\text{Swish}) - \text{FC}(1) - \text{B} - \text{Ac}(\text{Sigmoid})\}. \quad (4)$$

producing a scalar similarity in the range $[0, 1]$.

Similarity Learning and Optimization

Given an input pair (x_1, x_2) with a binary label y , where $y = 1$ denotes that x_1 and x_2 belong to the same class (“positive”) and $y = 0$ indicates they belong to different classes (“negative”), the SNN learns a shared transformation, parameterized by a

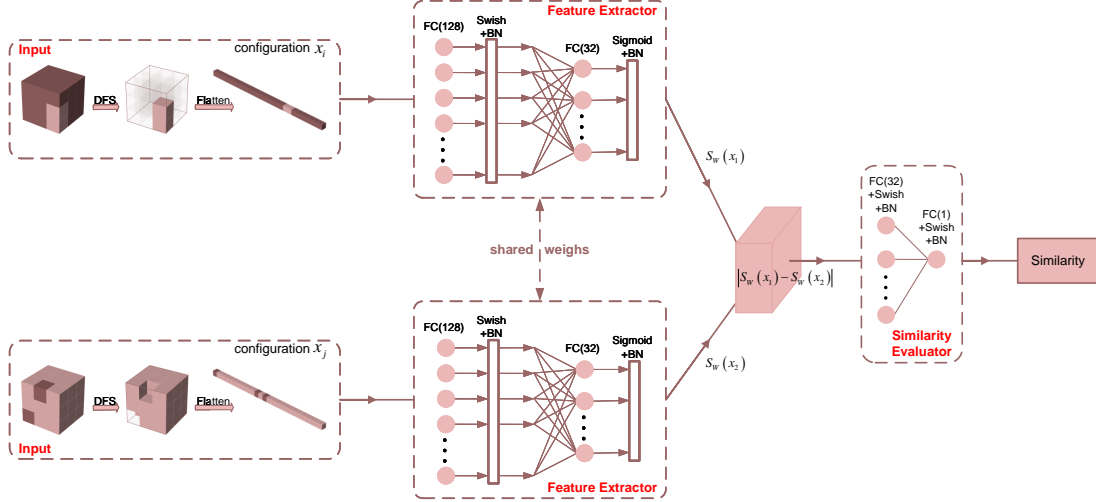


Figure 3. Schematic Diagram of the SNN Architecture.

weight matrix W , to map both inputs into a common latent representation space. A simplified form of the mapping can be expressed as:

$$S_W(x) = \sigma(Wx + b), \quad (5)$$

where σ is the activation function (e.g., Swish or Sigmoid), and b is the bias term. The distance between the latent representations $S_W(x_1)$ and $S_W(x_2)$ is then computed as:

$$D_W(x_1, x_2) = \|S_W(x_1) - S_W(x_2)\|. \quad (6)$$

This distance—or alternatively, the concatenated embeddings—is passed through a similarity evaluation network. The network outputs a scalar $s(x_1, x_2) \in [0, 1]$, representing the likelihood that the two inputs belong to the same phase.

Training and Loss Function

The SNN is trained using the binary cross-entropy loss function, defined as:

$$L = -\frac{1}{N} \sum_{i=1}^N [y(x_i, x_j) \log(s(x_i, x_j)) + (1 - y(x_i, x_j)) \log(1 - s(x_i, x_j))], \quad (7)$$

where N is the batch size, $y(x_i, x_j)$ is the ground-truth label for the i -th pair, and $s(x_i, x_j)$ is the predicted similarity. During backpropagation, the gradient of the loss with respect to the weights W is computed as:

$$\frac{\partial L}{\partial W} = \frac{1}{N} \sum_{i=1}^N \left[(s(x_i, x_j) - y(x_i, x_j)) \cdot \frac{\partial s(x_i, x_j)}{\partial W} \right], \quad (8)$$

enabling the optimization of W to minimize the loss and improve model performance.

4. Result

4.1 Monte Carlo Results

Prior to conducting ML analysis, we performed Monte Carlo simulations on 3D site and bond percolation models defined on cubic lattices to validate the reliability of the generated configurations. Simulations were carried out for system sizes $L = 10, 16, 20, 24$, and 30 , generating 1000 independent samples per occupation probability p to reduce statistical uncertainties.

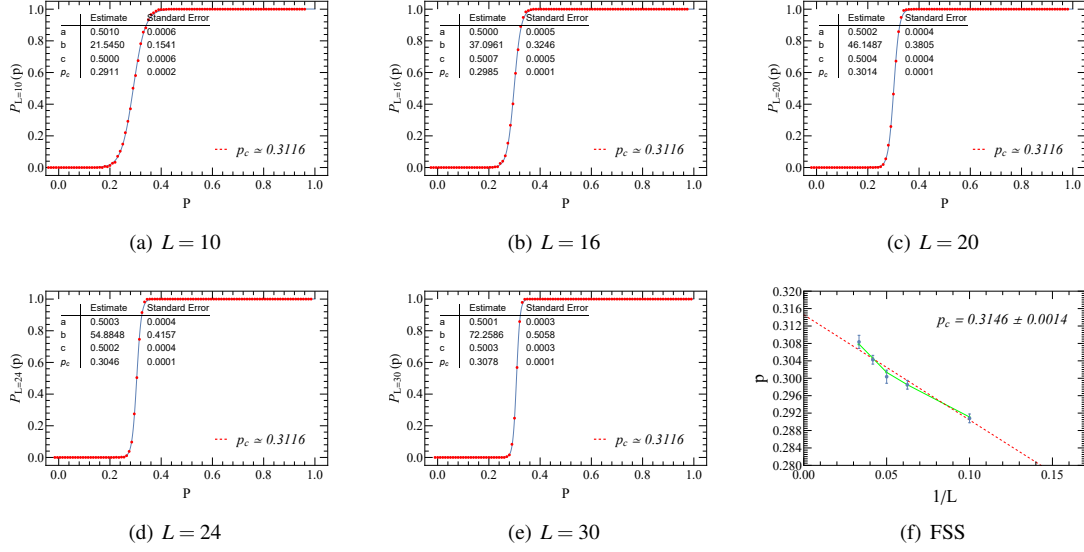


Figure 4. Monte Carlo simulation results for the 3D site percolation model. Panels (a)–(e) show results for system sizes $L = 10, 16, 20, 24$, and 30 , respectively. The estimated critical threshold p_c and its associated uncertainty are indicated in the upper-left corner of each subfigure. All sigmoid fits achieve a goodness of fit exceeding 99.9%. Panel (f) presents the extrapolation of p_c to the thermodynamic limit using FSS.

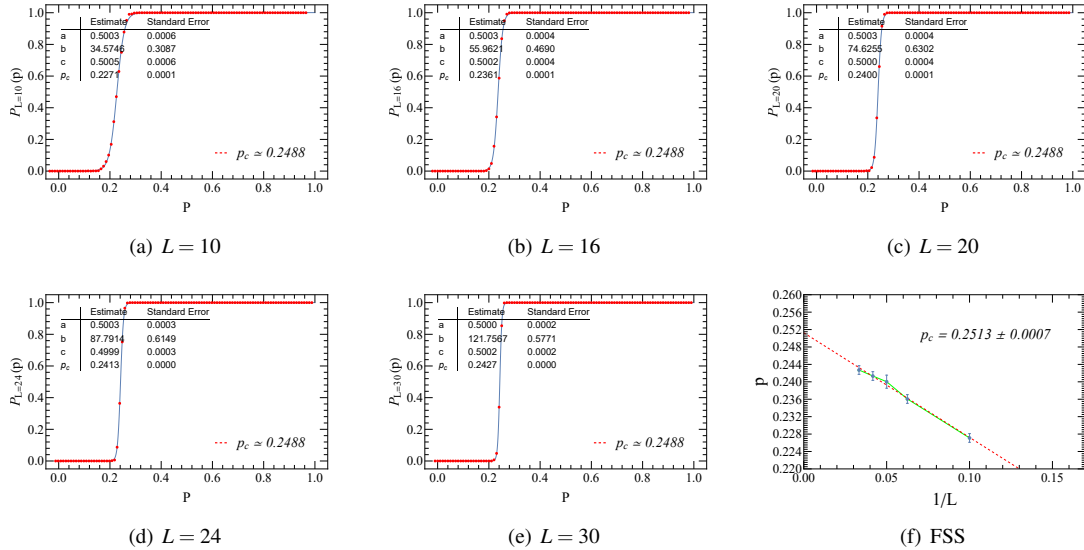


Figure 5. Monte Carlo simulation results for the 3D bond percolation model. Panels (a)–(e) show results for system sizes $L = 10, 16, 20, 24$, and 30 , respectively. The estimated critical threshold p_c and its associated uncertainty are indicated in the upper-left corner of each subfigure. All sigmoid fits achieve a goodness of fit exceeding 99.9%. Panel (f) presents the extrapolation of p_c to the thermodynamic limit using FSS.

The critical thresholds p_c for each system size were determined by fitting a Sigmoid function to the percolation probability curves, as illustrated in Figures 4(a)–(e) (site percolation) and 5(a)–(e) (bond percolation). The critical thresholds at the thermodynamic limit (infinite system size) were extrapolated via FSS, as shown in Figures 4(f) and 5(f), yielding estimates $p_c \simeq 0.3146(14)$ for site percolation and $p_c \simeq 0.2513(7)$ for bond percolation. These results align well with theoretical predictions ($p_c = 0.3116$ and $p_c = 0.2488$, respectively³¹), providing confidence in the validity of the simulation framework for downstream ML analysis.. Based on these verified datasets, we proceeded with further analysis using the SNN approach.

4.2 Input Data and Preprocessing for SNN

To facilitate the computational analysis and enable SNN-based learning, we generated binary tensor representations for the 3D site and bond percolation models:

Site percolation: $L \times L \times L$ binary tensors, where entries of 1 represent occupied sites and 0 represent vacant ones.

Bond percolation: $(2L + 1) \times (2L + 1) \times (2L + 1)$ binary tensors, where entries of 1 represent occupied bonds and 0 represent vacant bonds.

For each percolation probability p , 1000 independent configurations were generated and stored individually, resulting in 101 data points spanning the range $p \in [0, 1]$. The largest cluster from each configuration was extracted using the Depth-First Search (DFS) algorithm. These extracted configurations were subsequently used as input pairs for training and evaluating the SNN.

Labeling Strategy for Semi-Supervised Learning

This study adopts a semi-supervised learning framework for training the SNN, where only a small subset of the dataset is labeled. To minimize manual intervention and avoid introducing physical bias near the critical point, labeled samples were selected exclusively from the regions far from criticality, specifically the intervals $[0, 0.1] \cup [0.9, 1]$. This strategy resulted in only 22 labeled probability points across multiple system sizes.

Unlike traditional supervised learning that assigns labels to individual samples, the SNN adopts a pairwise labeling strategy. Labels are assigned to configuration pairs based on their relative similarity or dissimilarity. Specifically, two probabilities p_i and p_j are randomly sampled from within the intervals $[0, 0.1]$ and $[0.9, 1]$, respectively. The corresponding configurations x_i and x_j are then paired for similarity evaluation. The pair is labeled as:

- Positive: if x_i and x_j belong to the same interval, either $[0, 0.1]$ or $[0.9, 1]$;
- Negative: if x_i and x_j are sampled from different intervals.

To prevent sampling bias, the pool of 1000 configurations at each p value were independently shuffled prior to pair generation.

Training Process

1. The selected configurations x_i and x_j are input to the two branches of the SNN feature extractor, which maps them to latent representations $S_W(x_i)$ and $S_W(x_j)$.
2. The distance $D_W(x_i, x_j)$ between the latent embeddings is computed (Eq. 6) and used as input to the similarity evaluator.
3. The similarity evaluator outputs a scalar similarity $s(x_i, x_j)$, obtained by applying a Sigmoid activation to the final layer.
4. Model parameters are optimized by minimizing the binary cross-entropy loss function (Eq. 7) via backpropagation.

Testing Phase

1. A reference occupation probability p serving as the anchor, is randomly selected. A configuration x_i is then sampled from a test probability $p_i \in [0, 1]$ and paired with the anchor.
2. The SNN computes the similarity $s(x_p, x_i)$ between the anchor configuration x_p and the test configuration x_i .
3. By plotting the similarity $s(x_p, x_i)$ as a function of p_i , the critical threshold p_c is identified as the intersection point between the average similarity curves of positive and negative sample pairs.

4.3 SNN Results

In the three-dimensional site percolation model, an anchor probability of $p_a = 0.47$ was selected as the reference for similarity evaluation. The similarity computed by the SNN for various system sizes is shown in Figure 6(a). The results indicate that the similarity curve remains relatively stable in the intervals $[0, 0.2]$ and $[0.4, 1]$, but exhibits a sharp rise within $[0.2, 0.4]$. This interval is identified as the phase-transition region. The critical threshold in the thermodynamic limit, denoted as p_c^∞ , was estimated using FSS, as shown in Figure 6(b). Similarly, for the three-dimensional bond percolation model with an anchor probability of $p_a = 0.12$, the similarity curves and the estimated threshold p_c^∞ are presented in Figures 6(d) and 6(e), respectively. For both site and bond percolation models, the predicted critical thresholds are in good agreement with the theoretical values^{31,43}.

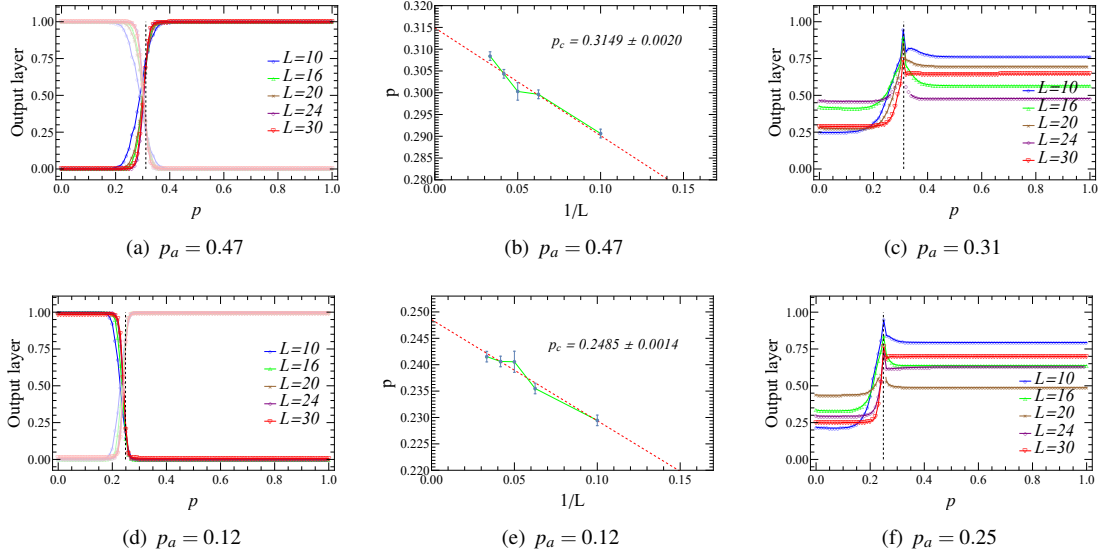


Figure 6. The first row shows results for the three-dimensional site percolation model: (a) Similarity (dark) and dissimilarity (light) curves for various system sizes at anchor $p_a = 0.47$; (b) FFS extrapolation for anchor $p_a = 0.47$; (c) Output layer responses for various system sizes at anchor $p_a = 0.31$, where the similarity curve peaks near the critical threshold $p_c \approx 0.31$. The second row shows results for the three-dimensional bond percolation model: (d) Similarity (dark) and dissimilarity (light) curves for various system sizes at anchor $p_a = 0.12$; (e) FFS extrapolation for anchor $p_a = 0.12$; (f) Output layer responses for various system sizes at anchor $p_a = 0.25$, where the similarity curve peaks near $p_c \approx 0.25$.

To assess the impact of anchor selection on prediction accuracy, multiple anchors were chosen from non-critical (non-phase-transition) regions for evaluation (see Tables 1 and 2). The critical thresholds summarized in the table indicate that variations in anchor selection have only a minor effect on prediction accuracy, demonstrating the robustness of the model. On the other hand, slight fluctuations in the estimated critical threshold across system sizes are observed, likely due to finite-size effects, in accordance with the expectations of FSS theory. It is important to note that all selected anchors are deliberately positioned away from the critical threshold to avoid the emergence of spiking behavior, as illustrated in Figures 6(e) and 6(f). Interestingly, the appearance of such spikes near p_c also provides a useful indicator for estimating the width of the phase-transition region.

Table 1. Critical thresholds for the three-dimensional site percolation model under different anchors.

	10	16	20	24	30	p_c^∞
$p_a = 0$	0.2910	0.2995	0.2985	0.3019	0.3051	0.3103(19)
$p_a = 0.15$	0.2924	0.2990	0.2982	0.3016	0.3050	0.3090(20)
$p_a = 0.47$	0.2906	0.2996	0.3003	0.3043	0.3084	0.3149(20)
$p_a = 1$	0.2908	0.2998	0.3004	0.3043	0.3084	0.3147(20)

Table 2. Critical thresholds for the three-dimensional bond percolation model under different anchors.

	10	16	20	24	30	p_c^∞
$p_a = 0$	0.2296	0.2354	0.2405	0.2406	0.2415	0.2484(14)
$p_a = 0.12$	0.2295	0.2355	0.2405	0.2406	0.2415	0.2485(14)
$p_a = 0.38$	0.2285	0.2359	0.2427	0.2431	0.2439	0.2530(19)
$p_a = 1$	0.2285	0.2362	0.2427	0.2431	0.2438	0.2530(18)

Furthermore, data collapse analysis was performed on the SNN outputs corresponding to different anchors to assess whether the method can reliably extract the critical exponent ν . The corresponding results are shown in Figures 7 and 8. As shown in the figures, when the critical exponent is set to $\nu \approx 0.88$, the data curves corresponding to different anchors in both the three-dimensional site and bond percolation models collapse onto a single universal curve, in good agreement with the theoretical value $\nu = 0.8765^{17}$. These results indicate that anchor selection has minimal impact on the estimation of the critical

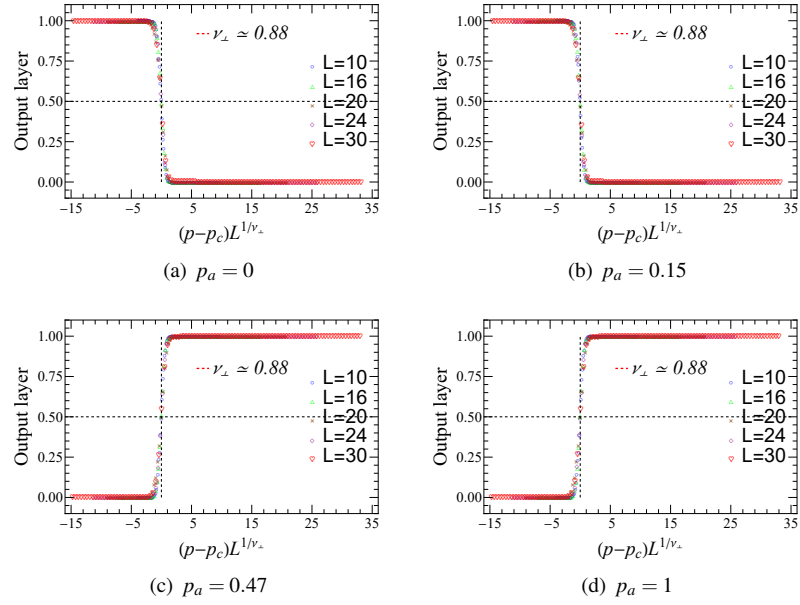


Figure 7. Data collapse analysis for estimating the critical exponent ν in the 3D site percolation model. Subfigures (a)–(d) correspond to anchor probabilities $p_a = 0, 0.15, 0.47$, and 1 , respectively.

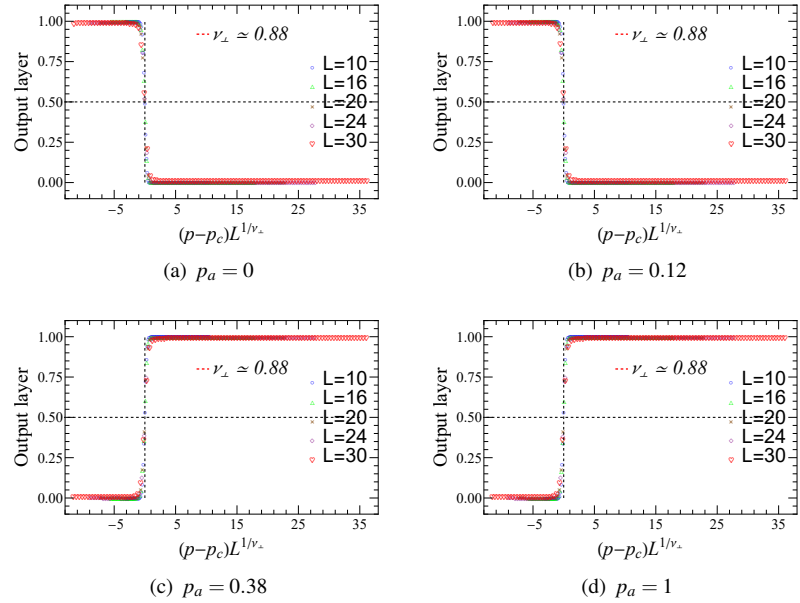


Figure 8. Data collapse analysis for estimating the critical exponent ν in the 3D bond percolation model. Subfigures (a)–(d) correspond to anchor probabilities $p_a = 0, 0.12, 0.38$, and 1 , respectively.

exponent ν , further demonstrating the robustness and effectiveness of the SNN approach in characterizing critical behavior in three-dimensional percolation models.

4.4 Extension of Data Labeling Range

As previously stated, the SNN follows a semi-supervised learning paradigm that requires manual labeling of a subset of the data during training. Inspired by previous work²⁷ and²⁸, we extend the labeling range to study its impact on prediction accuracy. Initially, the interval $[0, 0.1] \cup [0.9, 1]$ is used as the labeling range, and corresponding model outputs are obtained. Subsequently, the probability values $l^{(i)}$ and $r^{(i)}$ are identified as the points at which the similarity curve first falls below 99% and 1%, respectively. The initial probability boundaries $p^{(0)} = 0.1$ and $q^{(0)} = 0.9$ are iteratively updated, and the new labeling interval $[0, p^{(i)}] \cup [q^{(i)}, 1]$ is computed using Equation 9.

$$p^{(i)} = \frac{p^{(i-1)} + l^{(i-1)}}{2}, \quad q^{(i)} = \frac{q^{(i-1)} + r^{(i-1)}}{2} \quad (i = 1, 2, 3, \dots) \quad (9)$$

The iterative labeling process terminates once the condition $p^{(i)} = l^{(i)}$ or $q^{(i)} = r^{(i)}$ is satisfied. Figure 9(a) illustrates this iterative process for the 3D site percolation model with system size $L = 24$ and anchor $p_a = 0.47$. These intervals are selected because configurations within them predominantly belong to a single phase—either fully percolating or entirely non-percolating—and thus exhibit stable, non-critical behavior.

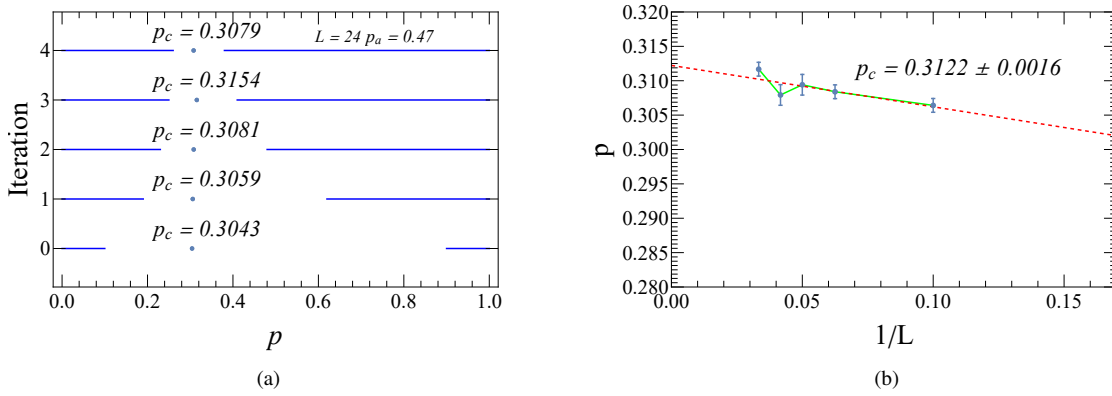


Figure 9. (a) Estimated critical thresholds at anchor $p_a = 0.47$ for the three-dimensional site percolation model with system size $L = 24$, obtained via iterative adjustment of the probability labeling range. (b) FSS extrapolation at anchor $p_a = 0.47$ as a function of $1/L$, based on the refined labeling interval.

We apply the aforementioned iterative method to determine the optimal labeling intervals for four selected anchors in the three-dimensional site percolation model across various system sizes, as summarized in Table 3. For all system sizes, the initial labeling interval is set to $[0, 0.1] \cup [0.9, 1]$, corresponding to iteration $i = 0$. All system sizes require four iterations to converge, except for $L = 16$, which converges after three iterations. Upon convergence, the critical thresholds corresponding to different anchors are estimated in the thermodynamic limit. The extrapolation for anchor $p_a = 0.47$ is shown in Figure 9(b), and the results for other anchors are listed in Table 4. Furthermore, a data collapse analysis is performed on the post-iteration data, and the corresponding estimates of the critical exponent ν are also reported in Table 4. In this table, the first and third rows present the results obtained before applying the iterative refinement, while the second and fourth rows correspond to the post-iteration outcomes.

Table 3. Iterative labeling ranges for the three-dimensional site percolation model.

	i=1	i=2	i=3	i=4
10	$[0, 0.15] \cup [0.64, 1]$	$[0, 0.18] \cup [0.51, 1]$	$[0, 0.19] \cup [0.45, 1]$	$[0, 0.20] \cup [0.39, 1]$
16	$[0, 0.18] \cup [0.62, 1]$	$[0, 0.22] \cup [0.49, 1]$	$[0, 0.24] \cup [0.42, 1]$	
20	$[0, 0.18] \cup [0.63, 1]$	$[0, 0.22] \cup [0.49, 1]$	$[0, 0.24] \cup [0.42, 1]$	$[0, 0.25] \cup [0.38, 1]$
24	$[0, 0.19] \cup [0.62, 1]$	$[0, 0.23] \cup [0.48, 1]$	$[0, 0.25] \cup [0.41, 1]$	$[0, 0.26] \cup [0.38, 1]$
30	$[0, 0.18] \cup [0.62, 1]$	$[0, 0.22] \cup [0.48, 1]$	$[0, 0.24] \cup [0.41, 1]$	$[0, 0.25] \cup [0.38, 1]$

Table 4. Comparison of critical thresholds and critical exponents for the three-dimensional site percolation model before and after iteration.

	$p_a = 0$	$p_a = 0.15$	$p_a = 0.47$	$p_a = 1$	MC	Literature
p_c	0.3103(19)	0.3090(20)	0.3149(20)	0.3147(20)	0.3146(14)	0.3116
p_c^{it}	0.3182(25)	0.3157(29)	0.3122(16)	0.3127(19)		
ν	0.88	0.88	0.88	0.88	0.88	0.8765
ν^{it}	0.88	0.88	0.88	0.88		

Comparison of the FSS and data collapse analyses before and after iteration reveals that extending the labeling interval does not significantly improve the accuracy in predicting either the critical threshold or the critical exponent. For instance, at anchor $p_a = 0.47$, the estimated critical threshold improved from $p_c = 0.3149(20)$ to $p_c = 0.3122(16)$ after refining the labeling interval. These findings suggest that the critical threshold and critical exponent of the three-dimensional percolation model can be accurately predicted, even with relatively narrow labeling intervals.

5. Conclusion

In this study, we systematically investigated the application of SNNs to site and bond percolation models defined on a three-dimensional cubic lattice. We first validated the configuration-generation procedure through Monte Carlo simulations. Using the validated configuration-generation algorithm, we generated percolation configurations and extracted the largest connected clusters using a DFS. We then applied SNNs to estimate the critical thresholds and critical exponents of the three-dimensional site and bond percolation models, demonstrating their effectiveness and robustness. The results show that the SNN approach, previously applied to two-dimensional systems, can be effectively generalized to three-dimensional models, maintaining high accuracy in identifying phase transitions despite the added complexity.

One of the key advantages of the SNN approach over traditional methods lies in its superior computational efficiency and predictive accuracy. In large-scale systems, where traditional approaches are often constrained by high computational costs, the SNN method exhibits notable improvements in scalability and performance. Furthermore, our analysis indicates that expanding the data labeling range does not necessarily lead to substantial improvements in prediction accuracy. For example, in the three-dimensional percolation model, extending the labeling range resulted in only minor deviations in the predicted critical thresholds and exponents. These findings suggest that the SNN approach can effectively predict phase transitions using a relatively limited set of labeled data, highlighting its practical utility in semi-supervised learning settings. Its reduced computational overhead and minimal labeling requirements make it especially well-suited for large-scale percolation studies.

This work makes several key contributions. First and foremost, it presents the first successful application of the SNN method for predicting critical thresholds in three-dimensional percolation models. This provides compelling evidence that SNNs, previously applied primarily to lower-dimensional or classification-focused problems, can also serve as effective tools for identifying phase transitions in complex, high-dimensional systems. Secondly, this study establishes a robust methodological framework that integrates machine learning with finite-size scaling analysis, thereby providing both theoretical and practical validation for applying neural network techniques to statistical physics. By highlighting the predictive power and computational efficiency of the SNN method, this work lays the foundation for the broader incorporation of machine learning into the study of critical phenomena.

From an application perspective, the SNN-based approach developed in this study shows strong potential. It can accurately predict the critical behavior of materials, potentially informing material design and engineering applications⁴⁴. Engineers and scientists could employ this approach to identify critical points⁴⁵, thereby optimizing material properties and supporting the development of more advanced and efficient materials. Moreover, this method can be applied to identify critical thresholds in complex networks, which plays a key role in understanding their structural stability and resilience. In fields such as geology and civil engineering, the SNN-based method can be used to analyze rock fracture and seepage phenomena⁴⁶. This capability may enhance the safety and efficiency of engineering systems.

In future work, we will continue exploring the synergy between machine learning techniques and classical statistical physics, with a particular emphasis on analyzing critical phenomena. One promising direction is to investigate how deep learning can be integrated with traditional methods—such as renormalization group theory and field-theoretic techniques—to refine the theoretical description of critical behavior^{47,48}. By leveraging the strengths of these complementary approaches, we aim to develop more accurate and comprehensive frameworks for describing phase transitions.

Moreover, the study of non-equilibrium phase transitions is expected to become a central research direction in statistical physics in the near future⁴⁹. Although significant progress has been made in the theoretical and numerical study of equilibrium phase transitions, modeling their non-equilibrium counterparts remains challenging due to their inherently non-stationary

and system-specific dynamics⁵⁰. Future efforts will therefore focus on improving existing algorithms and devising novel frameworks to tackle the unique challenges of non-equilibrium systems. These efforts aim to advance the field and provide deeper insights into the mechanisms governing such transitions.

In conclusion, the SNN-based framework introduced in this work serves as a robust and computationally efficient approach for investigating phase transitions in three-dimensional percolation models. Its applicability extends beyond the traditional scope of statistical physics, offering promising implications for a broad spectrum of fields, including materials science, complex networks, and geophysical systems.

Acknowledgements

This work was supported in part by the National Key Research and Development Program of China (Grant No. 2024YFA1611003); the Research Fund of Baoshan University (BYKY202305); Yunnan Fundamental Research Projects (Grant No. 202401AU070035); the Fundamental Research Funds for the Central Universities, China (Grant No. CCNU19QN029); the National Natural Science Foundation of China (Grant No. 61873104); the 111 Project 2.0 (Grant No. BP0820038); and the self-determined research funds of CCNU from the colleges' basic research and operation of MOE.

References

1. Alzubi, J., Nayyar, A. & Kumar, A. Machine learning from theory to algorithms: an overview. In *Journal of physics: conference series*, vol. 1142, 012012 (IOP Publishing, 2018).
2. Thiayalingam, J., Shankar, M., Fox, G. & Hey, T. Scientific machine learning benchmarks. *Nat. Rev. Phys.* **4**, 413–420 (2022).
3. Shalev-Shwartz, S., Shammah, S. & Shashua, A. Safe, multi-agent, reinforcement learning for autonomous driving. *Arxiv Prepr. Arxiv:1610.03295* (2016).
4. Char, D. S., Shah, N. H. & Magnus, D. Implementing machine learning in health care—addressing ethical challenges. *The New Engl. J. Medicine* **378**, 981 (2018).
5. Lin, W. Y., Hu, Y. H. & Tsai, C. F. Machine learning in financial crisis prediction: a survey. *IEEE Transactions on Syst. Man, Cybern. Part C (Applications Rev.)* **42**, 421–436 (2011).
6. Jordan, M. I. & Mitchell, T. M. Machine learning: Trends, perspectives, and prospects. *Science* **349**, 255–260 (2015).
7. Mohri, M., Rostamizadeh, A. & Talwalkar, A. *Foundations of machine learning* (The Mit Press, 2018).
8. Xue, T., Li, X., Chen, X., Chen, L. & Han, Z. Machine learning phases in swarming systems. *Mach. Learn. Sci. Technol.* **4**, 015028 (2023).
9. Hu, G. *et al.* Universality class of machine learning for critical phenomena. *Sci. China Physics, Mech. & Astron.* **66**, 120511 (2023).
10. Yang, Y. X. *et al.* Machine learning applications in phase transitions. *Sci. Sinica Phys. Mech. & Astron.* **53**, 290011 (2023).
11. Lifshitz, E. M. & Pitaevskii, L. P. *Statistical physics: theory of the condensed state*, vol. 9 (Elsevier, 2013).
12. Fishman, G. *Monte Carlo: concepts, algorithms, and applications* (Springer Science & Business Media, 2013).
13. Newman, M. E. J. & Ziff, R. M. Efficient monte carlo algorithm and high-precision results for percolation. *Phys. Rev. Lett.* **85**, 4104 (2000).
14. Hu, W., Singh, R. R. & Scalettar, R. T. Discovering phases, phase transitions, and crossovers through unsupervised machine learning: A critical examination. *Phys. Rev. E* **95**, 062122 (2017).
15. Van Nieuwenburg, E. P., Liu, Y.-H. & Huber, S. D. Learning phase transitions by confusion. *Nat. Phys.* **13**, 435–439 (2017).
16. Carrasquilla, J. & Melko, R. G. Machine learning phases of matter. *Nat. Phys.* **13**, 431–434 (2017).
17. Essam, J. W. Percolation theory. *Reports on progress physics* **43**, 833 (1980).
18. Pike, G. & Seager, C. Percolation and conductivity: A computer study. i. *Phys. review B* **10**, 1421 (1974).
19. Newman, M. & Ziff, R. M. Efficient monte carlo algorithm and high-precision results for percolation. *Phys. Rev. Lett.* **85**, 4104 (2000).
20. Ma, Y.-G., Pang, L.-G., Wang, R. & Zhou, K. Phase transition study meets machine learning. *Chin. Phys. Lett.* **40**, 122101 (2023).

21. Mehta, P. *et al.* A high-bias, low-variance introduction to machine learning for physicists. *Phys. Reports* **810**, 1–124 (2019).
22. Zhang, W., Liu, J. & Wei, T. C. Machine learning of phase transitions in the percolation and xy models. *Phys. Rev. E* **99**, 032142 (2019).
23. Li, X. *et al.* Machine learning phase transitions of the three-dimensional ising universality class. *Chin. Phys. C* **47**, 034101 (2023).
24. Patel, Z., Merali, E. & Wetzel, S. J. Unsupervised learning of rydberg atom array phase diagram with siamese neural networks. *New J. Phys.* **24**, 113021 (2022).
25. Wang, L. Discovering phase transitions with unsupervised learning. *Phys. Rev. B* **94**, 195105 (2016).
26. Wetzel, S. J. Unsupervised learning of phase transitions: From principal component analysis to variational autoencoders. *Phys. Rev. E* **96**, 022140 (2017).
27. Shen, J. M. *et al.* Transfer learning of phase transitions in percolation and directed percolation. *Phys. Rev. E* **105**, 064139 (2022).
28. Chen, X. N. *et al.* Study of phase transition of potts model with domain adversarial neural network. *Phys. A: Stat. Mech. its Appl.* **617**, 128666 (2023).
29. Chen, X. N. *et al.* Applications of domain adversarial neural network in phase transition of 3d potts model. *Phys. A: Stat. Mech. its Appl.* **637**, 129533 (2024).
30. Koch, G., Zemel, R., Salakhutdinov, R. *et al.* Siamese neural networks for one-shot image recognition. In *ICML deep learning workshop*, vol. 2, 1–30 (Lille, 2015).
31. Stauffer, D. & Aharoni, A. *Introduction to percolation theory* (Taylor & Francis, 2018).
32. Shante, V. K. & Kirkpatrick, S. An introduction to percolation theory. *Adv. Phys.* **20**, 325–357 (1971).
33. Saberi, A. A. Recent advances in percolation theory and its applications. *Phys. Reports* **578**, 1–32 (2015).
34. Isichenko, M. B. Percolation, statistical topography, and transport in random media. *Rev. modern physics* **64**, 961 (1992).
35. Araújo, N., Grassberger, P., Kahng, B., Schrenk, K. & Ziff, R. M. Recent advances and open challenges in percolation. *The Eur. Phys. J. Special Top.* **223**, 2307–2321 (2014).
36. Christensen, K. & Moloney, N. R. *Complexity and criticality*, vol. 1 (World Scientific Publishing Company, 2005).
37. Fessler, H. E. & Macklem, P. T. Percolation and phase transitions. *Am. J. Respir. Critical Care Medicine* **176**, 530–531 (2007).
38. Ranasinghe, T., Orăsan, C. & Mitkov, R. Semantic textual similarity with siamese neural networks. In *Proceedings of the international conference on recent advances in natural language processing (RANLP 2019)*, 1004–1011 (2019).
39. Chicco, D. Siamese neural networks: An overview. *Artif. neural networks* 73–94 (2021).
40. Zhang, C., Liu, W., Ma, H. & Fu, H. Siamese neural network based gait recognition for human identification. In *2016 IEEE international conference on acoustics, speech and signal processing (ICASSP)*, 2832–2836 (IEEE, 2016).
41. Taigman, Y., Yang, M., Ranzato, M. & Wolf, L. Deepface: Closing the gap to human-level performance in face verification. In *Proceedings of the IEEE conference on computer vision and pattern recognition*, 1701–1708 (2014).
42. Manocha, P. *et al.* Content-based representations of audio using siamese neural networks. In *2018 IEEE International Conference on Acoustics, Speech and Signal Processing (ICASSP)*, 3136–3140 (IEEE, 2018).
43. Deng, Y. & Blöte, H. W. Monte carlo study of the site-percolation model in two and three dimensions. *Phys. Rev. E* **72**, 016126 (2005).
44. Xie, T. & Grossman, J. C. Crystal graph convolutional neural networks for an accurate and interpretable prediction of material properties. *Phys. review letters* **120**, 145301 (2018).
45. Peixoto, T. P. Bayesian stochastic blockmodeling. *Adv. network clustering blockmodeling* 289–332 (2019).
46. Wang, N., Chang, H. & Zhang, D. Deep-learning-based inverse modeling approaches: A subsurface flow example. *J. Geophys. Res. Solid Earth* **126**, e2020JB020549 (2021).
47. Koch-Janusz, M. & Ringel, Z. Mutual information, neural networks and the renormalization group. *Nat. Phys.* **14**, 578–582 (2018).
48. Li, S.-H. & Wang, L. Neural network renormalization group. *Phys. review letters* **121**, 260601 (2018).

49. Henkel, M. *Non-equilibrium phase transitions* (Springer, 2008).
50. Täuber, U. C. *Critical dynamics: a field theory approach to equilibrium and non-equilibrium scaling behavior* (Cambridge University Press, 2014).